

IMPERIAL

EARLY STAGE ASSESSMENT

Flow transition over surface gaps in 2D incompressible laminar boundary layers

Author:

Víctor Ballester*

Supervisors:

Spencer Sherwin*

Yongyun Hwang*

Jeffrey Crouch†

Abstract

This study investigates the transition of flow over surface gaps in two-dimensional incompressible laminar boundary layers, with particular emphasis on the influence of small surface discontinuities on aerodynamic performance. The research is motivated by the increasing demand for fuel-efficient aircraft designs, where even minor geometric irregularities can significantly affect the onset of laminar–turbulent transition and thereby increase aerodynamic drag. Using **Nektar++**, an open-source high-fidelity spectral/ hp element solver, we solve the incompressible Navier–Stokes equations to examine how variations in gap geometry influence boundary-layer stability. Transition prediction is performed using the classical e^N -method, which characterizes the amplification of Tollmien–Schlichting waves. Numerical results are validated against experimental data, showing strong agreement. The analysis demonstrates that both gap width and depth critically affect flow stability, with direct implications for surface design in next-generation low-drag aircraft. The study concludes with proposed extensions to compressible flows and three-dimensional configurations to better capture transition phenomena in more realistic flight conditions.

Department of Aeronautics
Imperial College London

August 13, 2025

*Department of Aeronautics, Imperial College London.

†The Boeing Company, USA.

Contents

1	Introduction	1
2	Numerical framework	2
2.1	Numerical implementation	2
2.2	Domain and boundary conditions	4
2.3	Solving the linear systems	6
3	Linear stability analysis	7
3.1	e^N -method	8
4	Results	8
4.1	Direct numerical simulations	8
4.2	Δn factors comparison	10
5	Future work	11
	References	13

1. Introduction

Aircraft wings are not perfectly smooth; instead, they often exhibit small surface discontinuities, commonly referred to as gaps. These gaps may arise due to manufacturing tolerances (e.g., clearances around fasteners such as screws or rivets), structural assembly features (e.g., spanwise joints between skin panels), or the presence of movable control surfaces such as flaps, slats, or ailerons. Although these discontinuities are typically small in scale, they can significantly affect the development of the boundary layer, particularly its transition from laminar to turbulent flow. Since laminar–turbulent transition is a major contributor to skin-friction drag, even localized disturbances can meaningfully influence overall aerodynamic performance.

To date, few studies have systematically investigated the effects of surface gaps on boundary-layer transition. Most of them rely on the n -factor method, originally introduced by Smith and Gamberoni [18] and Van Ingen [19]. This method uses the relation $n(x) = \log(A(x)/A_0)$ to quantify the exponential growth of small disturbances of initial amplitude A_0 as they travel downstream. According to this framework, transition is assumed to occur when the amplification factor n exceeds a critical value, typically between 5 and 12, depending on the free-stream turbulence and other environmental conditions.

ONERA (*Office National d’Études et de Recherches Aéronautiques*) has recently conducted several experimental, numerical, and theoretical studies on the influence of surface gaps on boundary-layer behavior. The work by Béguet et al. [1] provides a comprehensive summary of these investigations. Gap geometry is characterized in terms of w/δ^* and d/δ^* , where w and d denote the width and depth of the gap, respectively, and δ^* is the displacement thickness of the boundary layer. Their study classifies vortex structures forming within the gap as functions of w and d , focusing on gaps with aspect ratios $d/w \in [0.2, 0.7]$. Regarding the n -factor, the authors adopt the notation $\Delta N = N - N_0$, where N denotes the n -factor for the gapped configuration and N_0 corresponds to the smooth flat-plate case. They report two primary effects: first, surface gaps amplify pre-existing Tollmien–Schlichting (TS) waves, as evidenced by increases in ΔN downstream of the gap; second, the gaps generate localized instabilities, leading to a peak in ΔN at the gap location. All these results were obtained under incompressible flow conditions.

Zahn and Rist [20] performed numerical simulations to examine the influence of deep gaps ($d/w \geq 5$) in compressible boundary-layer flows at a Mach number of $Ma = 0.6$. They observed non-monotonic behavior of ΔN as a function of gap depth, with values ranging from 0 to 0.5.

One of the most recent and detailed investigations was conducted by Crouch et al. [5], who extensively analyzed the amplification of TS waves over gaps with varying widths and depths. They found that for shallow gaps ($d/w < 0.017$), the ΔN factor depends primarily on the gap depth d and is independent of the width w . Conversely, for deep gaps ($d/w > 0.028$), the ΔN is governed by the gap width. When both d and w are sufficiently large, the TS-wave-induced transition is bypassed entirely, and the flow transitions to turbulence near the downstream edge of the gap. Their results also suggest that the behavior of shallow gaps resembles that of isolated backward-facing steps.

In this work, we investigate the influence of surface gaps on boundary-layer transition using a combination of direct numerical simulations and linear stability theory in the incompressible regime. As a validation step, we aim to reproduce and interpret the experimental findings of Crouch et al. [5], employing high-order numerical tools capable of resolving the growth of small-scale instabilities. Our ultimate goal is to develop a computational framework that accurately captures transition phenomena induced by surface gaps and can later be extended to compressible and three-dimensional flows (see Section 5).

The transition modeling follows the classical e^N approach, where linear perturbations (typically TS waves) are tracked as they amplify downstream through the laminar boundary layer. Transition is assumed to occur when the integrated disturbance growth reaches a critical N value. From a computational standpoint, we solve the incompressible Navier–Stokes equations using the spectral/ hp element method, which combines the geometric flexibility of finite elements with the accuracy of spectral methods. All simulations are performed using the open-source **Nektar++** framework [13].

This report is organized as follows. In Sections 2 and 3, we present the theoretical and numerical foundations of our study, including the numerical implementation, boundary-layer theory, and the e^N transition model. In Section 4, we compare our simulation results with experimental data, analyze the amplification of instability waves over surface gaps, and assess the sensitivity of transition to geometric variations. Finally, in Section 5, we outline potential directions for future research, including compressible extensions and full three-dimensional simulations.

2. Numerical framework

This work investigates the amplification of Tollmien–Schlichting (TS) waves in a two-dimensional, incompressible flow. The governing equations are the 2D incompressible Navier–Stokes equations, defined on a domain $\Omega \subset \mathbb{R}^2$. In dimensionless form, the equations read

$$\begin{aligned} \partial_t \mathbf{u} + (\mathbf{u} \cdot \nabla) \mathbf{u} &= -\nabla p + \nu \Delta \mathbf{u} \\ \nabla \cdot \mathbf{u} &= 0, \end{aligned} \tag{2.1}$$

where $\mathbf{u} = (u, v)$ denotes the velocity field, with u and v representing the horizontal and vertical velocity components, respectively; p is the pressure, and ν is the kinematic viscosity. These equations are supplemented by appropriate initial and boundary conditions. The system is non-dimensionalized by selecting the boundary-layer displacement thickness δ^* as the characteristic length scale. Specifically, we set $\delta_{ue}^* = 1$ at the upstream edge of the gap in a smooth surface without discontinuities. The reference velocity is taken as the free-stream velocity u_∞ at the top boundary. The corresponding Reynolds number based on δ^* is defined as

$$\text{Re}_{\delta^*} := \frac{u_\infty \delta_{ue}^*}{\nu} = \frac{1}{\nu}.$$

2.1. Numerical implementation

To solve the dimensionless equations (2.1), we employ a velocity-correction scheme implemented within a spectral- hp element framework, provided by the open-source library **Nektar++** [12].

Temporal discretization is performed using a second-order implicit-explicit (IMEX) splitting scheme [9], resulting in the semi-discrete form

$$\partial_t \mathbf{u}^{n+1} + \mathbf{N}(\mathbf{u}^{n+1}) = -\nabla p^{n+1} + \nu \Delta \mathbf{u}^{n+1}, \tag{2.2}$$

where $\mathbf{N}(\mathbf{u}^{n+1}) := (\mathbf{u}^{n+1} \cdot \nabla) \mathbf{u}^{n+1}$ is the nonlinear advection term. The time derivative is approximated using a second-order backward differentiation formula:

$$\partial_t \mathbf{u}^{n+1} = \frac{\alpha \mathbf{u}^{n+1} - \hat{\mathbf{u}}^n}{\Delta t}. \tag{2.3}$$

Here $\alpha = 3/2$ and $\hat{\mathbf{u}}^n := 2\mathbf{u}^n - \frac{1}{2}\mathbf{u}^{n-1}$. The nonlinear advection term is extrapolated as

$$\mathbf{N}^{n+1} = \mathbf{N}^{*,n+1} + \mathcal{O}(\Delta t^2), \quad \text{where } \mathbf{N}^{*,n+1} := 2\mathbf{N}^n - \mathbf{N}^{n-1} \tag{2.4}$$

to maintain second-order accuracy.

The velocity correction scheme proceeds in four stages:

1. Compute a temporary velocity field $\tilde{\mathbf{u}}^{n+1}$ which includes the nonlinear advection term:

$$\frac{\tilde{\mathbf{u}}^{n+1} - \hat{\mathbf{u}}^n}{\Delta t} = -\mathbf{N}^{*,n+1}. \quad (2.5)$$

2. Solve a Poisson equation for the pressure:

$$\Delta p^{n+1} = \frac{1}{\Delta t} \nabla \cdot \tilde{\mathbf{u}}^{n+1}. \quad (2.6)$$

3. Project the velocity onto a divergence-free space:

$$\frac{\bar{\mathbf{u}}^{n+1} - \tilde{\mathbf{u}}^{n+1}}{\Delta t} = -\nabla p^{n+1}, \quad \nabla \cdot \bar{\mathbf{u}}^{n+1} = 0. \quad (2.7)$$

4. Solve the Helmholtz equation for the updated velocity:

$$\frac{\alpha \mathbf{u}^{n+1} - \bar{\mathbf{u}}^{n+1}}{\Delta t} = \nu \Delta \mathbf{u}^{n+1} \implies \Delta \mathbf{u}^{n+1} - \frac{\alpha}{\nu \Delta t} \mathbf{u}^{n+1} = -\frac{1}{\nu \Delta t} \bar{\mathbf{u}}^{n+1}. \quad (2.8)$$

The corresponding boundary conditions are detailed in [Section 2.2](#). A schematic of the full time-integration loop is shown in [Fig. 1](#).

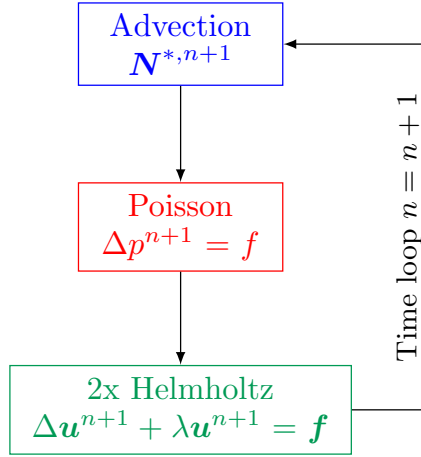


Figure 1: Schematic of each time step in the velocity correction scheme. Image extracted from [12].

Spatial discretization is carried out using a spectral- hp element method with a continuous Galerkin formulation. The discrete space of admissible velocity fields is defined as

$$\{\mathbf{u} \in H^1(\Omega) \times H^1(\Omega) : \mathbf{u} \in \mathcal{P}_p(\Omega) \times \mathcal{P}_p(\Omega)\}, \quad (2.9)$$

where $\mathcal{P}_p(\Omega)$ denotes the space of polynomials in Ω of degree at most p . A basis polynomials of this space are defined in the square $[-1, 1]^2$ and each basis function is formed as a tensor product $\phi_{ij}(x, y) = \phi_i(x)\phi_j(y)$ with ϕ_i being the i -th Legendre polynomial defined in $[-1, 1]$ [8]. For the sake of clarity, we will denote the basis functions simply as ϕ_i , with the index i ranging from 0 to $p^2 - 1$.

The weak form of (2.6) is obtained by testing with ϕ_i and using the divergence theorem:

$$-\int_{\Omega} \nabla \phi_i \cdot \nabla p^{n+1} + \int_{\partial\Omega} \phi_i \nabla p^{n+1} \cdot \mathbf{n} = \frac{1}{\Delta t} \int_{\Omega} \phi_i \nabla \cdot \tilde{\mathbf{u}}^n. \quad (2.10)$$

Similarly, the weak form of the Helmholtz equation (2.8) reads

$$-\int_{\Omega} \nabla \phi_i \cdot \nabla \mathbf{u}^{n+1} + \int_{\partial\Omega} \phi_i \nabla \mathbf{u}^{n+1} \cdot \mathbf{n} - \frac{\alpha}{\nu \Delta t} \int_{\Omega} \phi_i \mathbf{u}^{n+1} = -\frac{1}{\nu \Delta t} \int_{\Omega} \phi_i \bar{\mathbf{u}}^{n+1}. \quad (2.11)$$

These weak formulations result in linear systems whose solution is discussed in [Section 2.3](#).

2.2. Domain and boundary conditions

Following the approach of [10], we consider a rectangular computational domain with a sharp rectangular cavity (referred to as a gap) located on the bottom wall (see Fig. 2). The gap is fully characterized by its width w and depth d .

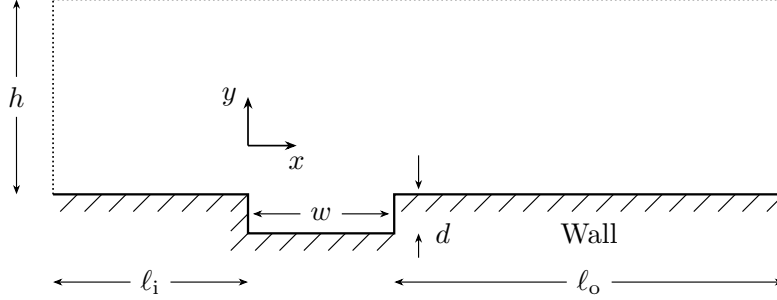


Figure 2: Computational domain. The dimensions have been heterogeneously rescaled to enhance visualization of the gap geometry.

The dimensions defining the domain are set as $h = 150\delta^*$, $\ell_i = 100\delta^*$, $\ell_o = 1000\delta^*$, with gap parameters $w/\delta^* \in [0, 130]$ and $d/\delta^* \in [0, 4]$. These values are chosen to ensure that all relevant physical phenomena are captured while keeping computational costs manageable.

The domain is discretized using N_e non-overlapping elements. The value N_e varies depending on the dimensions of the gap, but it is typically of the order of 10 000. Elements near the boundary layer are quadrilateral, while those farther from the wall, particularly near the top of the domain, are triangular. A schematic of the mesh is shown in Fig. 3. To satisfy the requirements of the continuous Galerkin method, a conforming mesh is used.

Quadrilateral elements are preferred in the boundary layer region due to their ability to support exact integration and differentiation operations, unlike triangular elements [8]. Triangular elements are placed outside the boundary layer region to allow for rapid expansion in element size. To mitigate the influence of the Courant–Friedrichs–Lewy (CFL) condition near the edges of the gap, the outer quadrilateral layer is locally reduced in extent, and the remaining region is discretized using triangular elements. This hybrid meshing strategy preserves high spatial resolution while permitting a larger time step in the numerical simulation.

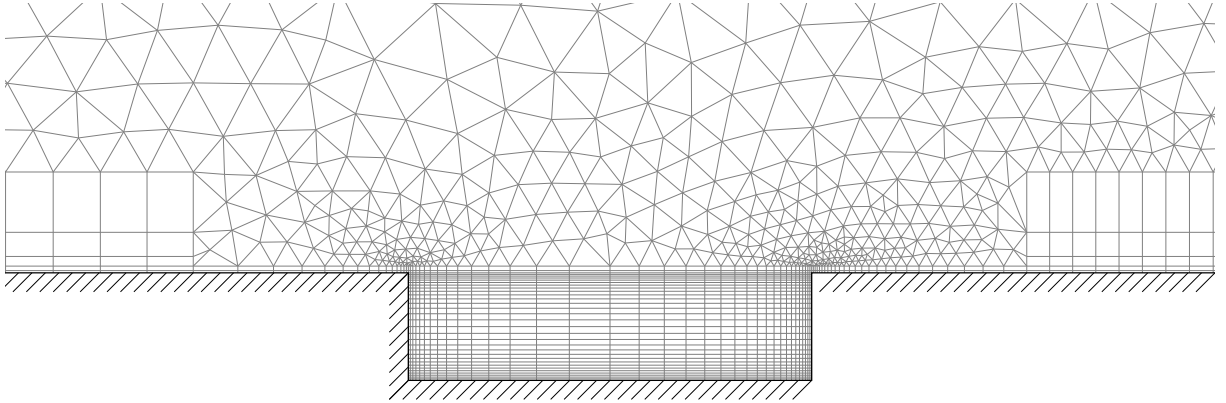


Figure 3: Zoomed-in, unscaled view of the mesh near the gap. The configuration shown corresponds to a gap with dimensions $w = 15\delta^*$ and $d = 4\delta^*$. The mesh is composed of quadrilateral elements near the boundary layer and triangular elements in the upper region. It is conforming and refined near the sharp corners of the gap.

The polynomial order is set to $p = 6$ for the velocity and $p = 5$ for the pressure. This choice, assigning one polynomial degree higher to the velocity field, ensures satisfaction of the inf-sup (Ladyzhenskaya–Babuška–Brezzi) condition [7, 13], which guarantees the existence and uniqueness of solutions to the Stokes problem.

Boundary conditions are imposed on all four sides of the domain: inflow (left), outflow (right), top, and bottom.

At the inflow, a fully developed Blasius boundary layer profile is prescribed. The Blasius profile is a self-similar solution of the boundary layer equations for incompressible, 2D, flat-plate flow with zero pressure gradient, i.e., $\partial_x p = 0$. The governing boundary layer equations in this case are

$$\begin{aligned} u\partial_x u + v\partial_y u &= \nu\partial_{yy} u \\ \partial_x u + \partial_y v &= 0. \end{aligned} \quad (2.12)$$

Blasius showed that these equations admit a self-similar solution through the substitution [2]

$$\begin{aligned} \eta &= y\sqrt{\frac{u_\infty}{\nu x}} \\ f(\eta) &= \frac{\psi}{\sqrt{\nu u_\infty x}}, \end{aligned} \quad (2.13)$$

where ψ is the streamfunction defined by $u = \partial_y \psi$, $v = -\partial_x \psi$. From this formulation, the velocity components become

$$\begin{aligned} u &= u_\infty f'(\eta), \\ v &= \frac{1}{2} \frac{u_\infty}{\sqrt{\text{Re}_x}} (\eta f'(\eta) - f(\eta)), \end{aligned} \quad (2.14)$$

where $\text{Re}_x := u_\infty x / \nu$ is the Reynolds number based on the distance from the leading edge of the plate.

Substituting (2.14) into the x -momentum equation in (2.12) yields the classical Blasius equation,

$$f''' + \frac{1}{2} f f'' = 0. \quad (2.15)$$

The equation is defined in $\eta \in [0, \infty)$ and it is equipped with boundary conditions derived from (2.14): $f(0) = 0$, $f'(0) = 0$, and $\lim_{\eta \rightarrow \infty} f'(\eta) = 1$.

This third-order ODE is solved using `solve_bvp` from the `scipy` Python library [3], which implements a fourth-order collocation method solved iteratively using Newton's method. As the resulting velocity profile cannot be directly imported into `Nektar++`, we fit it using rational functions of degree 11, ensuring that the relative error in the C^1 norm

$$\|f\|_{C^1} := \|f\|_\infty + \|f'\|_\infty \quad (2.16)$$

remains below 10^{-5} . The resulting fit reads

$$\tilde{u}_{\text{BL}}(\eta) = \begin{cases} \frac{p(\eta)}{q(\eta)} & \text{if } \eta < \eta_{\text{max}}, \\ u_\infty & \text{if } \eta \geq \eta_{\text{max}}, \end{cases} \quad (2.17)$$

where $p, q \in \mathcal{P}_{11}(\mathbb{R})$ and $\eta_{\text{max}} = 12$ is the cutoff point for the fit. A similar fit is constructed for the wall-normal velocity component. The resulting relative errors are

$$\frac{\|\tilde{u}_{\text{BL}}(\eta) - u\|_{C^1}}{\|u\|_{C^1}} < 10^{-5}, \quad \frac{\|\tilde{v}_{\text{BL}}(\eta) - v\|_{C^1}}{\|v\|_{C^1}} < 10^{-5}. \quad (2.18)$$

To impose a consistent pressure boundary condition at the inflow that preserves the time accuracy [11], we take the dot product of (2.2) with the normal vector \mathbf{n} to obtain

$$\partial_{\mathbf{n}} p^{n+1} = (\nu \Delta \mathbf{u}^{n+1} - \partial_t \mathbf{u}^{n+1} - \mathbf{N}(\mathbf{u})^{n+1}) \cdot \mathbf{n}. \quad (2.19)$$

Using the vector identity $\Delta \mathbf{u} = \nabla(\nabla \cdot \mathbf{u}) + \nabla \times \nabla \times \mathbf{u}$ and enforcing incompressibility (up to the time accuracy set, in this case $\mathcal{O}(\Delta t^2)$), we arrive at a high-order Neumann boundary condition,

$$\partial_{\mathbf{n}} p^{n+1} = (\nu \nabla \times \nabla \times \mathbf{u}^{*,n+1} - \partial_t \mathbf{u}^{*,n+1} - \mathbf{N}(\mathbf{u})^{*,n+1}) \cdot \mathbf{n}. \quad (2.20)$$

At the outflow, the simplest choice is to impose fully developed flow conditions, i.e., $\partial_{\mathbf{n}} \mathbf{u} = 0$ and $p = 0$. However, this can become unstable in the presence of energetic vortices [12, 6]. An alternative, more stable pressure Dirichlet condition is proposed in [6] as

$$p^{n+1} = \nu \mathbf{n} \cdot \nabla \mathbf{u}^{*,n+1} \cdot \mathbf{n} - \frac{1}{2} \|\mathbf{u}^{*,n+1}\|^2 S(\mathbf{n} \cdot \mathbf{u}^{*,n+1}), \quad (2.21)$$

where $S(\mathbf{n} \cdot \mathbf{u}) = \frac{1}{2}(1 - \tanh(\mathbf{n} \cdot \mathbf{u}/(\mathbf{u}_0 \varepsilon)))$ is a smooth step function, \mathbf{u}_0 is a reference velocity, and ε controls the steepness of the step.

Once p^{n+1} is known, the velocity at the boundary is set via

$$\mathbf{u}^{n+1} = \frac{1}{\nu} \left[p^{n+1} \mathbf{n} + \frac{1}{2} \|\mathbf{u}^{*,n+1}\|^2 S(\mathbf{n} \cdot \mathbf{u}^{*,n+1}) \mathbf{n} - \nu \nabla \mathbf{u}^{*,n+1} \cdot \mathbf{n} \right]. \quad (2.22)$$

At the top boundary, we impose free-stream conditions: $u = u_\infty$, $v = v_\infty(x)$, and the pressure condition from (2.20). We stress that the wall-normal velocity is x -dependent, as inherited from the Blasius profile. On the bottom wall, a no-slip condition is applied: $u = 0$, $v = 0$, and the pressure condition again follows (2.20), which reduces to the standard Neumann condition $\partial_{\mathbf{n}} p^{n+1} = 0$ in this case.

2.3. Solving the linear systems

In this section, we briefly outline the procedure used to solve the weak form of the pressure Poisson equation (2.10). The same approach applies analogously to the weak form of the velocity Helmholtz equation (2.11).

Integration is performed on an element-by-element basis. Let $\Omega_e \subset \Omega$ denote a single element. Using (2.10) together with the boundary condition from (2.20), the elementwise pressure equation becomes

$$\int_{\Omega_e} \nabla \phi_i \cdot \nabla p_e^{n+1} = -\frac{1}{\Delta t} \int_{\Omega_e} \phi_i \nabla \cdot \tilde{\mathbf{u}}_e^n + \int_{\partial \Omega_e} \phi_i (\nu \nabla \times \nabla \times \mathbf{u}_e^{*,n+1} - \partial_t \mathbf{u}_e^{*,n+1} - \mathbf{N}(\mathbf{u}_e)^{*,n+1}) \cdot \mathbf{n}, \quad (2.23)$$

where the subscript e indicates that the quantities are relative to the element Ω_e .

Assume that each physical element is obtained from a reference element via a mapping $\Omega_e = \varphi_e(\Omega_{\text{st}})$, where Ω_{st} refers to either the standard square element

$$\mathcal{Q}_{\text{st}} := \{(\eta_1, \eta_2) \in \mathbb{R}^2 : -1 \leq \eta_1, \eta_2 \leq 1\} \quad (2.24)$$

or the standard triangular element

$$\mathcal{T}_{\text{st}} := \{(\xi_1, \xi_2) \in \mathbb{R}^2 : -1 \leq \xi_1 \leq 1, -1 \leq \xi_2 \leq 1, \xi_1 + \xi_2 \leq 0\}. \quad (2.25)$$

It is noted that to construct tensor-product basis functions ϕ_i on \mathcal{T}_{st} , a collapsing-coordinates mapping is employed. One such mapping is given by

$$\xi_1 = \frac{(1 + \eta_1)(1 - \eta_2)}{2} - 1, \quad \xi_2 = \eta_2, \quad (2.26)$$

which maps the square \mathcal{Q}_{st} to the triangle \mathcal{T}_{st} as shown in Fig. 4.

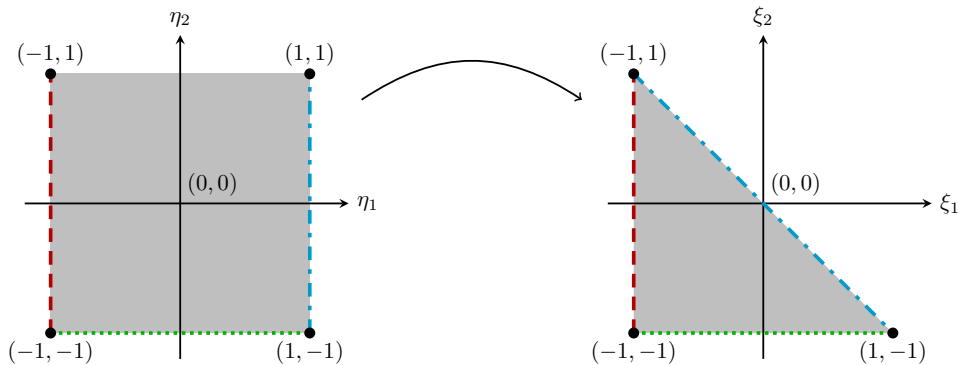


Figure 4: Collapsing-coordinates mapping from the standard square element \mathcal{Q}_{st} to the standard triangular element \mathcal{T}_{st} , as defined in (2.26). The line styles on the element edges illustrate how the boundaries are transformed under the mapping.

The pressure field is then expanded spectrally in terms of the basis functions as

$$p_e^{n+1} = \sum_{i=0}^{p^2-1} \hat{p}_{i,e}^{n+1} \phi_i. \quad (2.27)$$

Substituting this expansion into (2.23) yields the following linear system for each element

$$\mathbf{M}_e \hat{\mathbf{p}}_e^{n+1} = \mathbf{f}_e. \quad (2.28)$$

Here, $\mathbf{M}_e = (m_{ij}^e)$ is the elementwise mass matrix, defined as

$$m_{ij}^e = \int_{\Omega_{st}} \nabla \phi_i \cdot \nabla \phi_j J_e, \quad (2.29)$$

where $J_e = \mathbf{D}\boldsymbol{\varphi}_e$ is the Jacobian of the element mapping. In (2.28), $\hat{\mathbf{p}}_e^{n+1} = (\hat{p}_{i,e}^{n+1})$ is the vector of unknown pressure coefficients on element Ω_e , and $\mathbf{f}_e = (f_{i,e}^{n+1})$ is the corresponding right-hand side vector, assumed precomputed for brevity.

The entries m_{ij}^e are evaluated using Gauss quadrature with a sufficient number of points to ensure exact integration on quadrilateral elements. For more details on quadrature choices and integration accuracy, see [8]. In practice, the integral in (2.29) is approximated as

$$m_{ij}^e = \sum_{k=1}^{N_q} w_k \nabla \phi_i(\mathbf{x}_k) \cdot \nabla \phi_j(\mathbf{x}_k) J_e(\mathbf{x}_k) \quad (2.30)$$

where \mathbf{x}_k are the quadrature points and w_k are the associated weights, typically the product of 1D Gauss–Legendre weights for tensor-product elements.

Due to the continuous Galerkin formulation, certain degrees of freedom (DoFs) are shared between adjacent elements. To define the global system, let

$$p_{\text{gl}}^{n+1} = \sum_{i=0}^{N_{\text{dof}}-1} \hat{p}_{i,\text{gl}}^{n+1} \phi_i, \quad (2.31)$$

and introduce the global coefficient vector $\hat{\mathbf{p}}_{\text{gl}}^{n+1} = (\hat{p}_{i,\text{gl}}^{n+1})$, and the local coefficient vector $\hat{\mathbf{p}}_{\text{loc}}^{n+1} = (\hat{p}_{i,e}^{n+1})_{\substack{0 \leq i < p^2 \\ 0 \leq e < N_e}}$. Then, the global and local vectors are related via an assembly operator

$$\hat{\mathbf{p}}_{\text{loc}}^{n+1} = \mathcal{A} \hat{\mathbf{p}}_{\text{gl}}^{n+1}, \quad (2.32)$$

where \mathcal{A} is a sparse Boolean matrix (consisting of zeros and ones) that encodes the connectivity between local and global DoFs. Using this relation, we construct the global mass matrix \mathbf{M}_{gl} , which is assembled from the local elemental mass matrices. These local contributions are combined according to the assembly matrix, resulting in shared entries that reflect the continuity of degrees of freedom across element boundaries. For detailed information on the implementation and mathematical formulation of the spectral-*hp* element method, refer to [8]. This leads to a linear system of the form

$$\mathbf{M}_{\text{gl}} \hat{\mathbf{p}}_{\text{gl}}^{n+1} = \hat{\mathbf{f}}_{\text{gl}}^{n+1}, \quad (2.33)$$

which must be solved at each time step.

3. Linear stability analysis

We initiate the nonlinear simulations using a smooth initial condition. Depending on the gap geometry, the flow may evolve towards a steady state or display sustained oscillatory behavior. In cases where the solution converges to a steady flow, denoted by $\mathbf{U}(x, y)$, this state can be used as a critical point to perform a linear stability analysis around it.

To study the evolution of small-amplitude perturbations, we decompose the velocity field as

$$\mathbf{u}(x, y, t) = \mathbf{U}(x, y) + \mathbf{u}'(x, y, t), \quad (3.1)$$

where $\mathbf{u}' = (u', v')$ denotes the perturbation field, and u' and v' are the perturbation components in the streamwise and wall-normal directions, respectively. Substituting this decomposition into the full Navier–Stokes equations and retaining only terms linear in \mathbf{u}' , we obtain the linearized Navier–Stokes equations:

$$\begin{aligned} \partial_t \mathbf{u}' + (\mathbf{U} \cdot \nabla) \mathbf{u}' + (\mathbf{u}' \cdot \nabla) \mathbf{U} &= -\nabla p' + \nu \Delta \mathbf{u}' \\ \nabla \cdot \mathbf{u}' &= 0. \end{aligned} \quad (3.2)$$

Unless otherwise stated, we hereafter omit the prime notation and denote the perturbation field simply as \mathbf{u} .

3.1. e^N -method

The e^N method is a widely used approach in linear stability theory to quantify the amplification of disturbances in a flow. Its main assumption is that a perturbation of amplitude (yet to be defined) $A(x_0)$ at a reference position x_0 evolves in the streamwise direction x according to

$$A(x) = A(x_0)e^{n_{x_0}(x)}, \quad (3.3)$$

where $n_{x_0}(x)$ denotes the n -factor, which can be recovered from

$$n_{x_0}(x) = \log \left(\frac{A(x)}{A(x_0)} \right). \quad (3.4)$$

Henceforth, we omit the subscript x_0 for simplicity. A suitable definition for the amplitude in the wall-normal direction remains to be specified. In our setup, we choose the L^∞ norm of the velocity magnitude \mathbf{u} ,

$$A(x) := \|\mathbf{u}(x, y)\|_{L^\infty(\mathcal{Y}(x))} = \max_{y \in \mathcal{Y}(x)} |\mathbf{u}(x, y)| = \max_{y \in \mathcal{Y}(x)} \sqrt{u(x, y)^2 + v(x, y)^2}, \quad (3.5)$$

where $\mathcal{Y}(x)$ denotes the wall-normal domain at a given streamwise position x . Since the perturbation vanishes at the boundaries and the solution remains bounded, the maximum value is guaranteed to be attained within the domain.

4. Results

This section is divided into two main parts, corresponding to the principal contributions of this work. The first part presents the results of direct numerical simulations (DNS) of the incompressible flow over surface gaps with varying geometric configurations, specifically changes in gap width and depth. The second part focuses on the comparison between the numerically computed n -factors and experimental measurements reported in [5].

4.1. Direct numerical simulations

We performed a series of direct numerical simulations of boundary-layer flow over surface gaps of varying geometries. All results are obtained for a Reynolds number of $\text{Re}_{\delta^*} = 1000$. The results are summarized in Fig. 5.

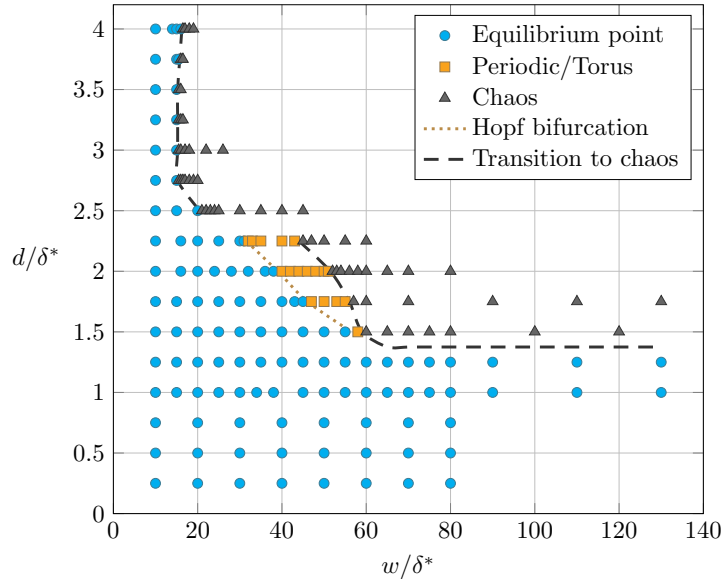


Figure 5: Stability diagram showing the dynamical regimes for different gap configurations at $\text{Re}_{\delta^*} = 1000$. Gap width w is shown along the horizontal axis and gap depth d along the vertical axis. Blue circles denote steady solutions (equilibria), orange squares represent time-periodic attractors, and black triangles indicate chaotic or turbulent states. The dotted orange line indicate a qualitative boundary for the first Hopf bifurcation while the dashed black line indicate the transition to chaos.

Blue markers indicate equilibrium solutions of the Navier–Stokes equations, i.e., steady states to which the system converges. As expected, small gaps (either in width or depth) yield stable flows resembling those over a flat plate, corresponding to the limiting cases $w \rightarrow 0$ or $d \rightarrow 0$.

The internal flow topology within the gap varies with its geometry. Outside the gap, the boundary layer retains a Blasius-like structure. Inside the gap, however, the behavior depends significantly on the available space. Representative steady-state solutions for three different configurations are shown in Fig. 6. Contours of the wall-normal velocity are displayed along with streamlines to visualize the internal flow structure.

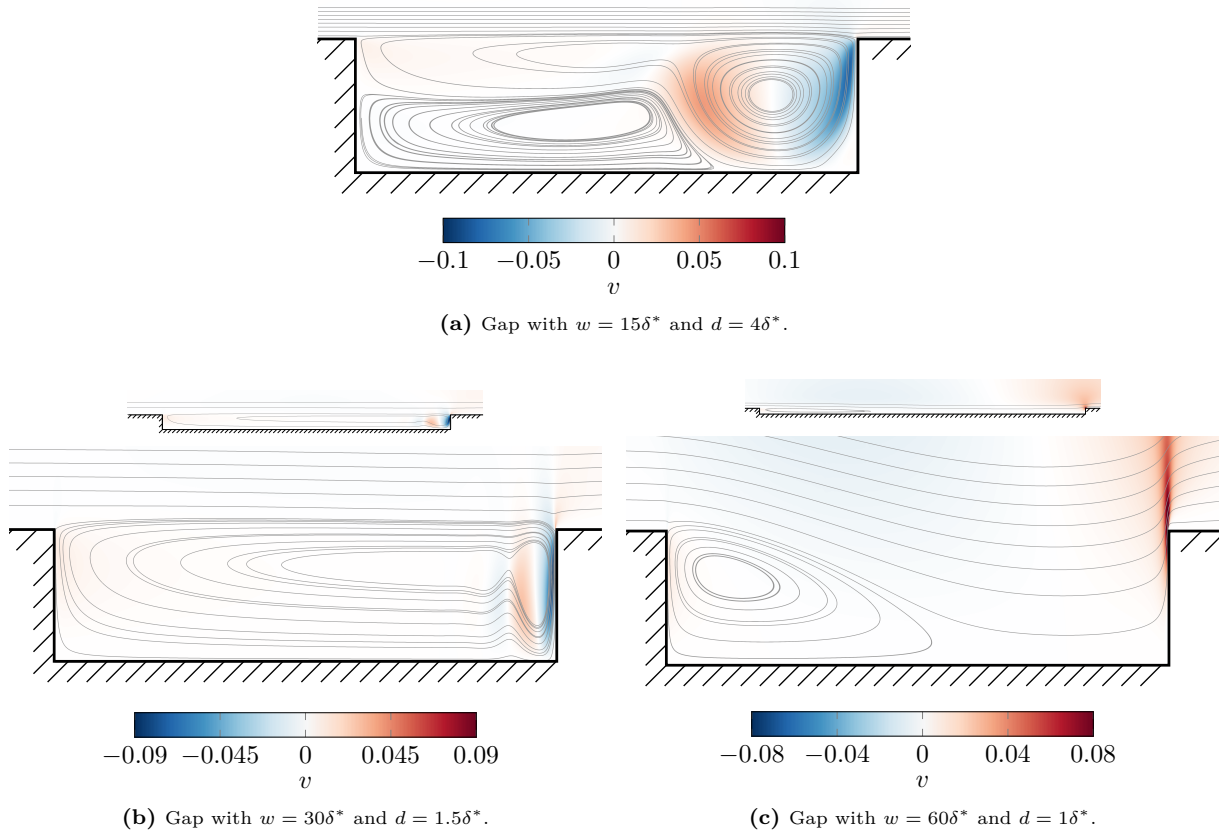


Figure 6: Steady-state flow over three different gap configurations. Wall-normal velocity contours and streamlines are shown in each case. All geometries are rescaled to match the size of the first configuration ($w/d = 15/4$) for visual comparison. The original, unscaled geometries are displayed above the last two cases for reference.

The configurations illustrated in Fig. 6 correspond to $(w/\delta^*, d/\delta^*) \in \{(15, 4), (30, 1.5), (60, 1)\}$. We observe that for deep gaps, a prominent recirculating region forms near the downstream edge of the cavity. In contrast, shallow gaps do not accommodate such structures; the flow instead enters and exits the cavity more smoothly, exhibiting a weak recirculation zone near the upstream edge.

For fixed gap depth, increasing the width induces a sequence of bifurcations. When the width surpasses a critical threshold that depends on the depth, the flow becomes unstable. For deep gaps ($d/\delta^* \in [2.5, 4]$), this transition occurs abruptly, while shallower configurations ($d/\delta^* \in [1.5, 2.25]$) exhibit a linearly unstable regime. In this latter region, a Hopf bifurcation emerges, introducing one unstable frequency. A second frequency appears soon after, producing quasiperiodic dynamics on a two-dimensional attracting torus. Spatially, this corresponds to an unstable global mode whose amplitude is concentrated near the downstream edge of the gap, as illustrated in Fig. 7.

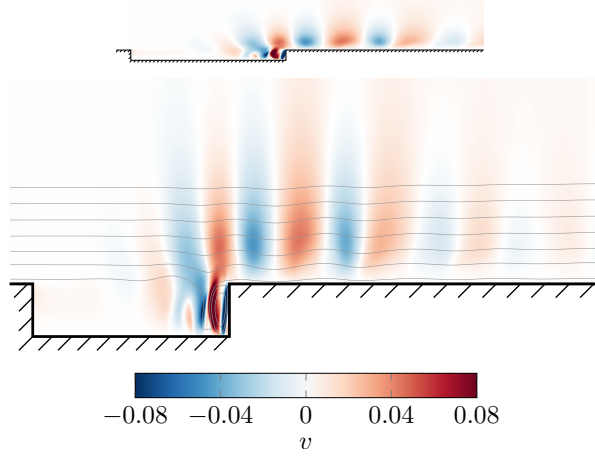


Figure 7: Self-sustained absolute instability near the downstream edge of a gap with $w = 35\delta^*$ and $d = 2.25\delta^*$. Wall-normal velocity contours are shown. The geometry is rescaled to $w/d = 15/4$. The original shape is shown above for reference.

As the width increases further, the attracting torus becomes increasingly distorted. Additional frequencies become less stable, leading ultimately to a chaotic regime [15].

4.2. Δn factors comparison

Based on the DNS results, we identify several steady baseflows \mathbf{U} that serve as a foundation for linear stability analysis (see Eq. (3.2)). Using each base flow, we solve the linearized Navier–Stokes equations given in Eq. (3.2). The numerical setup used for this analysis differs from the previous simulations. Since the baseflow already satisfies the boundary conditions, we impose homogeneous boundary conditions of the same type as before. To excite Tollmien–Schlichting (TS) waves, a small perturbation in the wall-normal velocity is introduced at the upstream region of the boundary layer. This perturbation is modeled as white Gaussian noise. Specifically, the wall-normal velocity component is defined as

$$v(x, t) = Ae^{-w(x-x_0)^2} X_t \quad (4.1)$$

where $A = 0.01$, $w = 5$, $x_0 = -95\delta^*$, and X_t represents a unit-variance white Gaussian noise process. The Gaussian function with the specific weight chosen localizes the excitation to a region of approximately $2\delta^*$ in length, centered at x_0 . While real experimental disturbances are neither white nor Gaussian, this idealized model is commonly employed for its simplicity and general applicability.

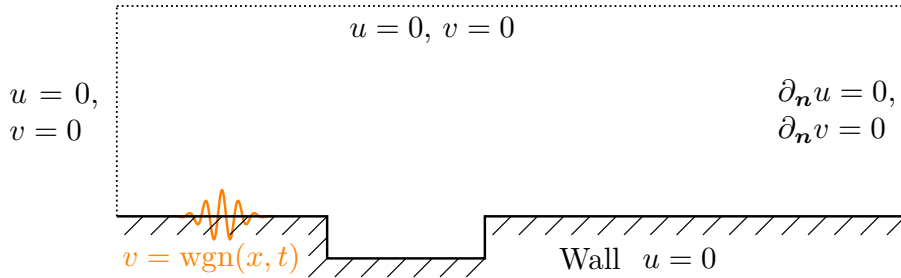


Figure 8: Schematic of the domain used in the stability analysis. White Gaussian noise is introduced in a small band at the upstream region to excite TS waves.

Since the perturbation is random, so is its amplitude. Therefore, before computing the maximum in Eq. (3.5), we use a time-averaged quantity based on the root-mean-square (RMS) of the velocity components:

$$A(x) = \max_{y \in \mathcal{Y}(x)} \sqrt{\langle u_i(x, y)^2 + v_i(x, y)^2 \rangle}. \quad (4.2)$$

Here, (u_i, v_i) are the streamwise and wall-normal components of the perturbation velocity at different time instances, and $\langle \cdot \rangle$ denotes the average over time.

After introducing the forcing, the flow requires a short transient period to stabilize. After this period, the relative perturbation amplitude reaches approximately 5×10^{-4} in the streamwise component and 5×10^{-2} in the wall-normal component. Simulations are run for a sufficient duration to allow temporal averaging over a set of control points, thereby suppressing stochastic fluctuations.

The minimum perturbation amplitude upstream of the gap is identified and used to compute the n -factor curve, $n_{\text{wgn}}(x)$, according to Eq. (3.4). For simplicity, we drop the subscript and refer to this simply as $n(x)$.

To compare with the experimental data of Crouch et al. [5], we compute the difference between the n -factor of each gapped configuration and that of the flat-plate reference case. Since this difference depends on the streamwise coordinate x , and our primary interest lies in the amplification of TS waves induced by the gap itself rather than its downstream evolution, we focus on a region of length $100\delta^*$ located after the onset of monotonic growth in the n -factor curves. We then average the n -factors over this interval to obtain a representative amplification value. This difference is denoted by Δn , rather than ΔN as in some experimental studies [5, 4], to emphasize that we are comparing specific growth histories rather than optimal envelope values.

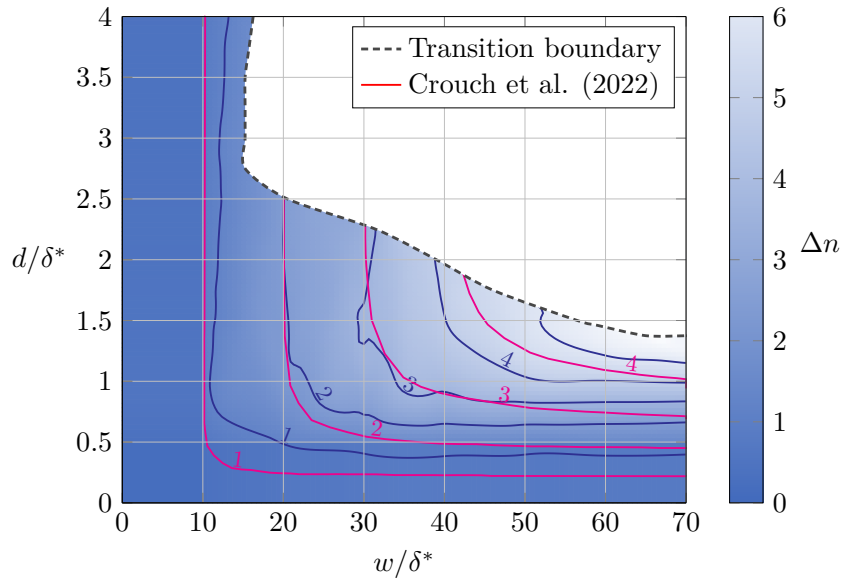


Figure 9: Contour plot of Δn factors on the stable side of the parameter grid $(w/\delta^*, d/\delta^*) \in [0, 70] \times [0, 4]$. Magenta contours show experimental level lines from [5] for levels 1, 2, 3, and 4.

The Δn values are computed at all gap configurations for which a steady baseflow was available. Interpolation is performed inside the convex hull of these points using linear interpolation, while nearest-neighbor extrapolation is applied outside the convex hull, but inside the globally stable region. To reduce artifacts from interpolation noise and the irregularities in the $n(x)$ curves, a Gaussian filter with $\sigma = 0.7$ is applied.

Overall, the comparison with experimental data (see Fig. 9) shows very good agreement. In particular, we correctly capture both asymptotic regimes: the vertical trend at narrow gaps and the horizontal trend at shallow gaps. We truncate the domain at $w = 70\delta^*$, since the amplification becomes large enough to invalidate the linearized Navier–Stokes approximation. Furthermore, simulations in the region $(w/\delta^*, d/\delta^*) \in [70, 140] \times [0, 1.25]$ were not extensively performed due to strict numerical stability constraints in the CFL number (see Fig. 5). For such cases where Δn is higher than 6, nonlinear effects would start becoming important, requiring a fully nonlinear perturbed boundary layer analysis to accurately capture saturation and transition mechanisms.

5. Future work

Future research will proceed along two primary directions. The first is the extension of the current analysis to compressible flows. The second involves generalizing the geometry to three dimensions in order to investigate the effects of spanwise instabilities.

Up to this point, this work has focused exclusively on incompressible flow, which is a valid approximation at low Mach numbers. However, many cruise conditions in aeronautical applications occur at moderate to high Mach numbers, where compressibility effects become significant. Extending the present framework to compressible flow will require substantial modifications. **Nektar++** provides a compressible Navier–Stokes solver that employs a discontinuous Galerkin method, the Flux Reconstruction approach, or the Interior Penalty method for spatial discretization. Time integration is performed using an implicit Runge–Kutta scheme, and the resulting nonlinear system is solved using a Newton iteration.

The inflow boundary condition must also be revised. In the compressible regime, a modified Blasius-type boundary layer profile is needed to maintain self-similarity. The appropriate similarity variable in this case is given by [17, 14]

$$\eta = \sqrt{\frac{u_\infty \rho_\infty}{\mu_\infty x}} \int_0^y \frac{\rho}{\rho_\infty}, \quad (5.1)$$

where ρ_∞ and μ_∞ denote the free-stream density and dynamic viscosity, respectively. When $\rho = \rho_\infty = 1$, this expression reduces to the incompressible case Eq. (2.13). However, due to the loss of linearity between η and y , interpolating the compressible Blasius profile for use as input to the solver becomes more challenging.

With regard to linear stability analysis and the computation of Δn -factors, we note that **Nektar++** currently lacks a linearized solver for the compressible Navier–Stokes equations. As a result, either a dedicated linear solver must be implemented, or the full nonlinear solver must be employed to evaluate amplification. While the latter approach is computationally more expensive, it may also yield more accurate results.

The second research direction concerns the inclusion of three-dimensional effects. This is motivated by the need to better understand the mechanisms that govern transition in swept-wing flows, where three-dimensional boundary layers play a critical role [16]. In this context, an additional parameter ϕ will be introduced to represent the sweep angle of the wing. The computational domain will be extruded in the spanwise direction using a Fourier expansion, resulting in a quasi-3D configuration. The sweep angle ϕ will correspond to the angle between the streamwise (u_∞) and spanwise (w_∞) components of the free-stream velocity.

Under this new setup, genuinely three-dimensional instabilities such as crossflow modes may arise. Additionally, gap-induced instabilities, such as the self-sustained absolute instability illustrated in Fig. 7, may exhibit different behavior in three dimensions, potentially transitioning from absolute to convective due to spanwise effects.

References

- [1] S. Beguet et al. “Modeling of Transverse Gaps Effects on Boundary-Layer Transition.” In: *Journal of Aircraft* 54.2 (2017), pp. 794–801. DOI: [10.2514/1.C033647](#).
- [2] H. Blasius. “Grenzschichten in Flüssigkeiten mit kleiner Reibung.” In: *Zeitschrift für Angewandte Mathematik und Physik* 56 (1908), pp. 1–37.
- [3] S. Community. *scipy.integrate.solve_bvp*. Accessed: 24/07/2025. SciPy Project. 2024. URL: [↗](#).
- [4] J. D. Crouch. “Predicting Laminar-Turbulent Transition Influenced by Surface-Induced Flow Distortions.” In: *IUTAM Laminar-Turbulent Transition*. Ed. by S. Sherwin, P. Schmid, and X. Wu. Cham: Springer International Publishing, 2022, pp. 19–32. ISBN: 978-30306-7-9-0-2-6.
- [5] J. D. Crouch et al. “Characterizing surface-gap effects on boundary-layer transition dominated by Tollmien–Schlichting instability.” In: *Flow* 2 (2022), E8. DOI: [10.1017/flow.2022.1](#).
- [6] S. Dong, G. E. Karniadakis, and C. Chrysosostomidis. “A robust and accurate outflow boundary condition for incompressible flow simulations on severely-truncated unbounded domains.” In: *Journal of Computational Physics* 261 (2014), pp. 83–105. DOI: [11.1016/j.jcp.2013.12.042](#). URL: [↗](#).
- [7] G. N. Gatica. *A Simple Introduction to the Mixed Finite Element Method: Theory and Applications*. Springer Briefs in Mathematics. Springer, 2014. ISBN: 978-33190-3-6-9-4-6.
- [8] G. Karniadakis and S. Sherwin. *Spectral/hp Element Methods for Computational Fluid Dynamics*. Oxford University Press, 2005. ISBN: 978-019-852-8-6-9-2. DOI: [10.1093/acprof:oso/9780198528692.001.0001](#).
- [9] G. E. Karniadakis, M. Israeli, and S. A. Orszag. “High-order splitting methods for the incompressible Navier-Stokes equations.” In: *Journal of Computational Physics* 97 (2 1991), pp. 414–443. DOI: [10.1016/0021-9991\(91\)90007-8](#). URL: [↗](#).
- [10] G. Lyu. *Transonic boundary layer transition prediction over wing sections with embedded DG spectral/hp discretisations*. Sept. 2023. DOI: [10.25560/109239](#). URL: [↗](#).
- [11] Nektar++ Consortium. *Nektar++: Spectral/hp Element Framework, Version 5.7.0 Developer Guide*. Version 5.7.0. Oct. 30, 2024. URL: [↗](#).
- [12] Nektar++ Consortium. *Nektar++: Spectral/hp Element Framework, Version 5.7.0 User Guide*. Version 5.7.0. Oct. 30, 2024. URL: [↗](#).
- [13] Nektar++ Consortium. *Spectral/hp Element Framework*. Accessed: 22/07/2025. URL: [↗](#).
- [14] F. Oz and K. Kara. “A CFD Tutorial in Julia: Introduction to Compressible Laminar Boundary-Layer Flows.” In: *Fluids* 6 (2021). DOI: [10.3390/fluids6110400](#).
- [15] D. Ruelle and F. Takens. “On the nature of turbulence.” In: *Communications in Mathematical Physics* 20 (1971), pp. 167–192. DOI: [10.1007/BF01646553](#).
- [16] W. S. Saric, H. L. Reed, and E. B. White. “Stability and transition of three-dimensional boundary layers.” In: *Annual Review of Fluid Mechanics* 35 (2003), pp. 413–440. DOI: [10.1146/annurev.fluid.35.101101.161045](#).
- [17] H. Schlichting and K. Gersten. *Boundary-Layer Theory*. 9th ed. Springer Berlin, Heidelberg, 2016. ISBN: 978-36625-2-9-1-8-4. DOI: [10.1007/978-3-662-52919-1](#).
- [18] A. M. O. Smith and N. Gamberoni. *Transition, Pressure Gradient and Stability Theory*. El Segundo Division, 1956.
- [19] J. L. van Ingen. *A suggested semi-empirical method for the calculation of the boundary layer transition region*. Report. Accessed 22/07/2025. Delft University of Technology, 1956. URL: [↗](#).
- [20] J. Zahn and U. Rist. “Impact of Deep Gaps on Laminar–Turbulent Transition in Compressible Boundary-Layer Flow.” In: *AIAA Journal* 54.1 (2016), pp. 66–76. DOI: [10.2514/1.J054112](#).